Techno-economic evaluation of a Brayton Battery configuration with Power-to-Heat extension

Sergej Belik

Institute of Engineering Thermodynamics, German Aerospace Center (DLR)
Stuttgart, Germany, Sergej.Belik@dlr.de

***Abstract*: The development of cost-efficient, environmentally friendly, and reliable technologies for utility-scale electricity storage is a key element for future flexible power systems. Brayton cycle-based Pumped Thermal Energy Storage (PTES) offers the potential of making a substantial progress to reach this goal. For further improvements in cost efficiency and flexibility we investigate the additional integration of Power-to-Heat (PtH) into the heat pump cycle. This integration allows a reduction in component size due to higher energy density; however, it also leads to efficiency losses. The objective of this paper is to quantify this tradeoff between round-trip efficiency and cost efficiency for closed-cycle Joule-Brayton PTES configurations and to provide design solutions for the novel PtH component. To this end, a wide-range design study with variable electric heating power and component efficiencies is conducted. In addition to the thermodynamic analysis, an economic assessment is presented, which clarifies the benefits of PtH extension. The results show a significant reduction of specific capital costs by up to 23%, along with higher system flexibility and a loss in round-trip efficiency of up to 5%.**

1 Introduction

The ongoing transformation of electrical energy systems from conventional to renewable energy supplies increases the need for energy storage technologies [1]. Large-scale electrical energy storage (EES) supports the integration of fluctuating renewable energy sources, which allows for a more reliable and flexible supply of low-carbon and zero-carbon electricity generation. However, EES technologies typically have significant drawbacks, such as capital costs, round-trip efficiency, cycle stability and locational dependency. To reduce these constraints, various technologies have been developed.

1.1 Established electric energy storage technologies

Pumped hydro energy storage (PHES) and diabatic compressed air energy storage (D-CAES) are established, large-scale EES technologies providing gigawatt hours of energy storage capacity for grid-scale peak leveling applications.

PHES is the most mature EES and benefits from high output power of 1.0 – 1.50 GW and high round-trip efficiency (RTE) in the range of 70% - 80% but suffers from locational dependency and high capital costs of 600 – 2000 $/kW [2, 3].

D-CAES technology is derived from a temporally decoupled multi-stage Brayton cycle in which air is compressed in an underground cavern during charging and mixed with natural gas for combustion in a modified gas turbine during the delivery period. Existing diabatic plant configurations operating in Huntorf (Germany) and McIntosh (USA) output 321 MW and 110 MW with an RTE of 42% and 54%, respectively [5]. The capital costs estimated for this storage technology range from 400 to 800 $/kW [4, 5]. In addition to the required geographical morphology, a major drawback of D-CAES technology is the low RTE accompanying the use of fossil fuels.

1.2 Adiabatic electric energy storage

Alternative thermo-mechanical EES technologies are currently being developed, namely, adiabatic CAES (A-CAES) and Carnot batteries (CB). Carnot batteries can be categorized into pumped thermal energy storage (PTES) and adiabatic liquid air energy storage (A-LAES). These storage technologies are adiabatic due to the integration of thermal energy storage (TES) following the polytropic compression process. The references [6-8] give a comprehensive overview of CB, while de Sisternes et al. [9] and Xue [10] show the state of the art of A-CAES and A-LAES. In addition, Benato et al. [5] focussed their study on PTES, which categorizes Rankine cycle-based (Rankine Carnot battery) and inverse Brayton cycle-based (Brayton Carnot battery) CBs. The essential performance characteristics of these adiabatic EES are summarized in Table 1.

A-CAES and A-LAES use TES to store compression heat during the charging period and transfer it during the delivery period to the heat engine process in a modified gas turbine. In contrast to D-CAES, the addition of TES results in a higher

Table 1. Comparison of large-scale adiabatic EES [10-29]

Adiabatic EES	**A-CAES (TRL 5-6)**	**A-LAES (TRL 7-9)**	**Brayton -PTES[1]**	**Rankine -PTES[2]**
Storage capacity [MWh]	1-1000	10-1000	1-1000	20-600
Power rating [MW]	0.5-90	0.35-100	0.5-150	1-100
RT efficiency [%]	60-75	45-65	45-67	25-64
Volumetric energy density [kWh/m^3]	0.5-20	50-80	20-70 (430)	10-22
CAPEX [$\$_{2021}$/kWh]	150-316	250-640	100-400	250-400
Lifetime [a]	20-40	20-40	25-30	25-30
Locational-dependency	Yes	No	No	No

[1] HT-regenerator based system using air as WF (TRL 2-5) [21, 23]
[2]Transcritcal Rankine PTES using CO_2 as WF (TRL 2-4) [13-16]

RTE in a range from 60 % to 75 % [11] and, as no additional fossil fuel is used, it operates without CO_2 emissions. The main benefit of A-LAES is the high energy density due to the low volume of liquefied air. Major drawbacks are the high capital expenditures (CAPEX) for A-LAES and geographical constraints for the air storage (aquifers and salt caverns) in the case of A-CAES [11, 12].

Nomenclature

a_v	specific surface area (m^{-1})
c_p	specific heat capacity (J kg^{-1} K^{-1})
H_0	magnetic field strength (A m^{-1})
H	total length (m)
k	heat transfer coefficient (W m^{-2} K^{-1})
m	storage mass (kg)
$\dot{m}_f$	mass flow rate (kg s^{-1})
P_{el}	electrical power input (W)
$\dot{Q}_{PtH}$	Joule heat induced by electrical heating (W)
$\dot{q}_{PtH}$	Joule heat power density (W m^{-3})
St	Stanton number
t	time scale (s)
T	temperature (K)
V	volume (m^3)
w_f	free flow velocity (m s^{-1})
w_t	specific technical work (J kg^{-1})
z	length scale (m)
Greek letters	
β	compression ratio (-)
ε	void fraction (-)
κ	fluid's isentropic exponent (-)
η_{PtH}	electric heating efficiency, $\dot{Q}_{PtH}/P_{el}$
λ	thermal conductivity (W m^{-1} K^{-1})
ρ	density (kg m^{-3})
τ	duration of charging/discharging period (s)
μ_0	magnetic field constant $4\pi 10^{-7}$(N A^{-2})
Γ	dimensionless heater loss number (-)
Λ	dimensionless heater length (-)
Π	dimensionless heater period duration (-)
Φ	dimensionless heat source number (-)
Ψ	thermal compression ratio (-)
$\dot{X}$	dimensionless exergy: $\dot{X}_{EFH} = \Phi\Lambda(1-\epsilon)$
Acronyms	
A/D-CAES	a/diabatic compressed air energy storage
A-LAES	adiabatic liquid air energy storage
CAPEX	capital expenditures (€)
CB	Carnot battery
EES	electrical energy storage
EFH	electric flow heater
HE / HP	heat engine / heat pump (cycle)
HT/LT	high-temperature / low-temperature
HX	heat exchanger
PTES	pumped thermal energy storage
PtH	power-to-heat
RTE	round-trip efficiency
STES	solid media thermal energy storage
ETES	electrically heated thermal energy storage
TM	turbomachinery
WF	working fluid

Subscripts and superscripts	
in / out	inlet / outlet
S / F	solid phase / fluid phase
p / poly	polytropic process
is	isentropic process
$'$	related to charging period (HP cycle)
$''$	related to discharging period (HE cycle)
$\overline{x}$	averaged quantity x
x^*	normalized quantity x

The Rankine Carnot battery uses various working fluids in dependence with the thermodynamic cycle. Transcritical Rankine battery uses CO_2, subcritical Rankine battery uses water, synthetic or organic fluids. In addition to the HCES concepts, Steinmann introduced Power to Heat to Power (PHP) concepts employing an ETES unit, which is heated completely by Joule heating in order to power the coupled Clausius Rankine cycle (CRC) or Organic Rankine cycle (ORC), for instance.

The Rankine Carnot battery, i.e. a Rankine PTES, uses a phase change working fluid (WF) to run the heat pump (HP) and the heat engine (HE) cycles. Rankine PTESs are categorized into transcritical and subcritical cycles according to their WF type. Transcritical Rankine battery uses CO_2 [13, 14], subcritical Rankine battery uses water (steam) [15] or organic fluids as WF. During charging the WF evaporates receiving the heat from the low-temperature (LT) reservoir. This gaseous WF compresses afterwards by the vapour compressor to high temperatures and pressures, accounting storage temperature of 123°C at 140 bar maximal pressure for the transcritical CO_2 cycle [14] and 365 °C at 105 bar for subcritical steam Rankine cycle [15]. Then, the WF condensates releasing the latent heat to the high-temperature (HT) TES before it finally expands to the initial state. During discharging, the thermal energy stored inside the HT-TES is used to evaporate the pressurized WF that later expands in a turbine to deliver technical work. Finally, the WF condensates releasing the heat to the LT-TES.

Another option for the Rankine Carnot battery system is the implementation of an electrically heated TES (ETES) [16] instead of the usually expensive heat pump for charging the HT-TES. This CB system has recently received attention for the purpose of retrofitting existing coal-fired power plants into EES [17]. Here, the electrically charged high-temperature heat of a sensible TES can be dispatched through the Rankine steam cycle. A resistive heater generates the HT heat for the sensible

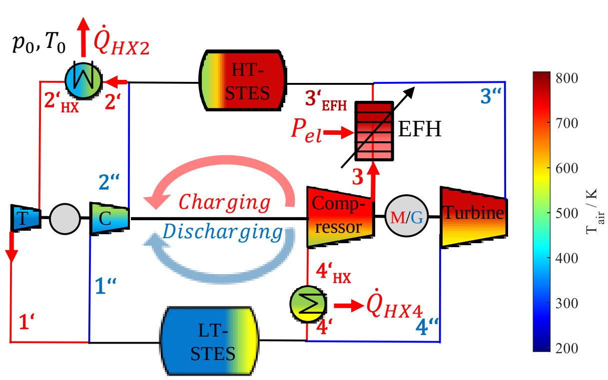

Fig. 1. Schematic of Brayton battery configuration with an electric flow heater (EFH); illustrated operation state is at the end of the charging period

molten salt TES with a maximum storage temperature of 560 °C [17].

The Brayton Carnot battery, i.e. a Brayton PTES has a similar working principle compared to the Rankine Carnot battery. In contrast to the phase change WF from Rankine CB systems, it employs a gaseous WF that is usually argon or air [5]. Here, the thermal energy is converted from electricity in a high-temperature HP cycle and stored inside two TESs, comprising a low- temperature and a high-temperature pressure vessel. The stored thermal energy is then reconverted into electrical energy using a gas turbine cycle. The residual heat from the gas turbine is stored in the low-temperature TES tank for feeding back into the Brayton HP cycle. Given this layout, the Brayton CB contains two thermal tanks and four turbomachines (two compressors and two expanders). Desrues et al. [23] first performed system simulations based on the Brayton cycle with a energy storage capacity of 602.6 MWh and a round-trip efficiency of 66.7 %. In comparison to other EES technologies, Brayton PTES benefits from its high energy density and low CAPEX. Additionally, this EES has no geographical constraints [5, 6].

From an economic standpoint, the current revenue options from energy arbitrage and frequency regulation are still too low to cover the high capital costs [11]. Therefore, cost efficiency and system flexibility need to be improved. One promising option for cost reduction alongside with gains in performance and flexibility is the implementation of an additional electric heating component downstream of the HP compressor [12].

1.3 Power-to-heat integration in A-CAES and Brayton CB

Adding a high-performance Power-to-Heat (PtH) unit into the heat pump cycle increases the thermal energy density of the system [18, 19, 21] that can be used to reduce the pressure ratio of turbomachines (TM) and hence to minimize their size. This allows for a lower pressure setting for the high-pressure stage while maintaining a high system temperature. Moreover, component size of TESs and heat exchangers can be minimized which consequently lowers their equipment costs without affecting system's power output [20, 24]. The main drawback of PtH integration is the reduction in round-trip efficiency (RTE) caused by the lower coefficient of performance (COP) during charging on the one hand, and the limited Carnot efficiency of the gas turbine cycle on the other hand [19-21].

Several research efforts have been carried out to investigate A-CAES and Brayton CB configuration concepts with additional PtH integration in terms of energy efficiency, cost efficiency and flexibility. For application in A-CAES, Dreissigacker et al. [19] found that the integration of PtH in the low-pressure stage upstream of the TES is associated with the least efficiency losses while Houssainy et al. [20] clearly showed the increase in storage density with a resulting decrease in system costs and efficiency through an ETES implementation in the high-pressure stage. Central results reveal major CAPEX reduction from 200 \$/kWh at 57.5% RTE to 65 \$/kWh at 24.5% RTE.

For the application in Brayton CB, Benato [18] and Chen et al. [21] proposed the integration of an electric heater between the HP compressor and HT-TES, as proposed in Fig. 1, with the aim of decoupling the compressor pressure from its outlet temperature. In doing so, Benato intended to reduce the costs of the HP compressor by limiting its capability. Therefore, the author limited the HP compressor pressure ratio to 6, thereby reducing its outlet temperature to 550 °C and raising the HT-TES inlet temperature up to 1050 °C using the electric heater. At this maximum storage temperature, Benato's techno-economic assessment for a TES build-up with Al_2O_3 brick indicates an energy density increase of 105% to 430 kWh/m^3, a CAPEX reduction of 35% to 54 \$/kWh, and an unexpected upgrade of the RTE from 6.3% to 7.0%. While efficiency is expected to fall with reduced system costs, low-cost turbomachines with a poor isentropic efficiency of 0.80 dominate the enormous drop in RTE below 10% [23, 25] and the overall system costs [26, 29]. Therefore, a temperature rise within the HE cycle might improve the RTE and reduce costs at such a low-efficiency level. Chen et al. [21] presented a similar system configuration and proposed to utilize the excess heat with a bottoming organic Rankine cycle (ORC). Since the excess heat temperature ranges from 550 K to 750 K, its exergy can be suitably dispatched through the ORC, improving the system's RTE to 47.1%. Although this RTE is 5.89% lower compared to the operation without an additional electric heater, the energy density is more than doubled to 62.2 kWh/m^3. In summary, all these studies show the effects of additional PtH integration into the thermo-mechanical and adiabatic EES, wherein energy density increases significantly and results in cost reduction accompanied by a slight loss in RTE.

1.4 Review of calculation methods

In the reviewed literature [18-21], the authors used similar methods for modeling the system and each component. Table 2 summarizes these approaches.

Different model complexities are implemented for component modeling depending on their individual characteristics. In all of the reviewed sources, turbomachinery and HX are modeled as stationary components. For the turbomachines, the isentropic state change is used to determine the outlet temperature. For the HX, practical NTU formulations [30, 31] are applied to determine its size. In contrast, the modeling of the TES and the electric heater has a different complexity. While Houssainy et al. [20] model the HT-TES together with the heater as a lumped capacity, assuming a constant temperature during discharging, Dreissigacker et al. [19] and Chen et al. [21] take into account the typical drop in outlet temperature for the regenerator-based HT-TES using a one-dimensional and two-phase thermal model for their design study. However, in both studies, as well as in [18], the electric heater is ideally considered a punctiform heat source inside the system, providing only the required energy demand for a given temperature increase of the WF. Benato [18] uses a one-dimensional thermal model from [32] to design the TES unit. In accordance with [20, 21], the author also assumes an ideal electric heater as a punctiform heat source without giving any details about its shape and dimension.

The system model connects the component models at the appropriate intersections for both the HP and HE cycles, and iterates until achieving cyclic equilibrium for HP and HE temperatures. Since WF properties change at each iteration and

TABLE 2. COMPARISON BETWEEN MODELING APPROACHES FROM REVIEWED LITERATURE (MODEL DIMENSIONS AND PHASES S : SOLID AND F :FLUID)

References	WF property database	TM	HX	TES	EFH
[18]	CoolProp	0d, ad.	NTU	1d; F	0d (Fluid)
[19]	CoolProp	0d, ad.	NTU	1d; S/F	0d (Fluid)
[20]	cal.perfect gas	0d, ad.	NTU	0d	0d (Fluid)
[21]	REFPROP	0d, ad.	NTU	1d; S/F	0d (Fluid)
This study	CoolProp	0d, ad.	NTU-ε	1d; S/F	1d (S/F)

in each cycle point with its temperature, the implementation of a material property database at the system level is necessary. Therefore, Benato [18], Dreissigacker et al. [19], and McTigue et al. [29] used the CoolProp database [27], while Chen et al. [21] implemented the REFPROP [28] database into the system-level simulation to calculate the temperature-dependant thermal properties of a real WF gas. Furthermore, Houssainy et al. [20] use formulations for mass and energy balance in combination with calorically perfect gas equations of state.

1.5 Contributions

In literature [18-21], the authors have carried out a technical evaluation and demonstrated the increase in energy density along with the decrease of component size through the implementation of a high-temperature EFH component into the adiabatic EES system. However, the EFH component is simply specified according to a given temperature rise [18, 21] or a required energy demand [19, 20]. As such, the shape and dimension of the component cannot be determined. Apart from Dreissigacker et al. [19], the authors further specify high-temperature requirements for the EFH without providing technical solutions: while an outlet temperature around 420-450 °C [19] is feasible for a two-stage A-CAES with available EFH technology, the Brayton CB requires considerably higher temperatures of up to 1050°C [18] or even more (1400 K) [21] with a lack of technical EFH solutions. Despite the mentioned lack of solutions, Benato [18] conducted a techno-economic evaluation that puts the cost of the EFH at $C_{\mathrm{EFH}} = 75000 \cdot P_{EFH}^{0.9}$ \$ /MW. Furthermore, as mentioned in section 1.3, the author demonstrates a cost reduction along with a slight improvement in RTE to 7.0%, where a tradeoff is normally expected. Therefore, the main objective of the present paper is to quantify this tradeoff between system costs and its efficiency that arises from the additional integration of PtH. The main hypothesis is that PtH offers a significant cost leverage when a compact EFH component is added downstream of the HP compressor. Another objective is to present a novel design solution for the EFH that meets the application-specific requirements of a Brayton CB. These essentially include a high cost and energy efficiency of over 85% at an outlet temperature above the maximum compressor temperature of 550°C [18].

The following contributions of this study are derived from above considerations:

- Provision of an efficient Brayton CB model employing component costs and real gas behavior for the WF
- Techno-economic system analysis quantifying the impact of the additional EFH on costs and efficiency
- Design study providing a design solution for the EFH component

To address these contributions, Section 2 first introduces a simplified modeling approach for a closed-cycle Brayton CB configuration with a PtH extension. Sections 3 and 4 describe the component models and the setup for system simulation. Results for wide-range parameter and design studies with increased PtH heating rates are presented in Section 5. In addition to the thermodynamic analysis, we conduct an economic assessment of these advanced Brayton CB configurations to demonstrate the effect of cost reduction through the PtH extension. Finally, Section 6 presents our study conclusions.

2 SYSTEM DESCRIPTION AND THERMODYNAMIC CYCLE ANALYSIS

2.1 Brayton CB with extended electric flow heater

The closed-loop system configuration from Fig. 1 without an electric heater component has been studied in various theoretical works [10, 33-37] where air has been used as WF. This system consists of one compressor and turbine pair for charging and another for the discharging period, two solid media thermal energy storage (STES) systems integrated in between the turbomachines, and two heat exchangers (HX). In addition, a motor and generator with associated clutches are needed to convert the electrical energy into mechanical energy and vice versa for the respective adiabatic compression and expansion processes.

In order to increase system energy density and cost efficiency, the electric flow heater (EFH) employed in [18] is integrated in the process scheme from Fig. 1 in the same manner. The red area in the associated temperature-entropy diagram from Fig. 2 illustrates the additional high-temperature heat given to the system. The integration downstream of the HP compressor has two technical reasons. First, the application of the EFH lowers the temperature requirements for the HP compressor, which has a maximum outlet temperature of 550°C. Second, the isobaric heating process of a pressurized gas (states 3'→3'$_{\mathrm{EFH}}$ in Fig. 2) generates a lower entropy rate compared to the isobaric heating at lower gas pressures. This makes the heating process more efficient from a Second Law perspective. Therefore, the combination of compression heat (4'$_{\mathrm{HX}}$→3') from the heat pump cycle and HT heat from the EFH (3'→3'$_{\mathrm{EFH}}$) is a feasible and exergetically efficient solution for generating HT heat for the Brayton heat engine cycle.

Two PtH technologies are worth considering for the EFH due to the high-power density and high efficiency required for the heating process: resistance heating and induction heating. Both operate on the principle of the Joule effect and provide high temperatures above 500 °C, which are required to efficiently run the closed-loop Brayton heat engine cycle. However, EFHs based on commercially available resistance heating elements are limited to outlet temperatures of 600 to 700 °C due to the limited heat transfer area of the tubular heating elements [38, 39]. To reach higher outlet temperatures, we propose a PtH concept that consists of an inductively heated and fluidized pebble bed [40]. In contrast to tubular heating elements, the pebble bed provides a 50% larger specific heat transfer area, which makes the convective heat transport of the inductively generated heat more efficient. Moreover, the contactless electric power transmission allows temperatures above 900 °C inside the pebble bed without being limited by electrical contacts. Therefore, we prefer to use the induction air heater that is based on a pebble bed concept for generating high-temperature heat for Brayton CB application.

To take advantage of the high-temperature potential of the induction air heater, we propose the combination with a counterflow regenerator STES [22]. The high-temperature and low-temperature STES regenerators are comprised of thermally insulated pressure vessels with a ceramic honeycomb inventory. The honeycomb inventory concept allows maximum operating temperatures of up to 1200 °C [32]. The direct contact heat transfer between the WF air and the honeycomb inventory leads to an efficient heat transport provided by the large heat transfer area. Additionally, the large diameter of the storage tanks results in low air velocities, which lead to low-pressure losses.

The HXs used in the study are common counterflow shell-and-tube type HXs that use water as a coolant. These are installed downstream of each STES and are operated only during the charging period to take advantage of the low-cost electricity running the water pumps.

2.2 *Thermodynamic cycle analysis*

The thermodynamic analysis aims at discussing the impact of PtH integration on the performance of the Brayton CB configuration from Fig. 1. To derive a general conclusion on the storage systems' performance, we chose the discharged specific technical work $w_{t,HE}$ of the Brayton HE cycle (blue area in Fig. 2: 1”→2”→3”→4”→1”) as the key performance metric. Assuming ideal gas behavior of the working fluid and an adiabatic system with a reversible heat transport inside the STES and HX components, only the turbomachine irreversibility needs to be considered. Based on these assumptions, we apply polytropic process equations to the HP (notation ‘) and HE cycles (notation ’’) of Fig. 2. using the thermal compression ratio Ψ and the polytropic efficiency η_p to calculate the outlet temperature of turbomachinery:

$$T_{1'} = T_{2',HX} \cdot \Psi_{turb}^{-\eta_{p,turb}} \quad \text{and } T_{1''} = T_{1'} \tag{1}$$

$$T_{2''} = T_{1'} \cdot \Psi_{comp}^{\frac{1}{\eta_{p,comp}}} \tag{2}$$

$$T_{3'} = T_{4',HX} \cdot \Psi_{comp}^{\frac{1}{\eta_{p,comp}}} \tag{3}$$

$$T_{4''} = T_{3''} \cdot \Psi_{turb}^{-\eta_{p,turb}} \quad \text{and } T_{3',EFH} = T_{3''} \tag{4}$$

The EFH outlet temperature $T_{3',EFH}$ may be expressed using the dimensionless exergy rate $\dot{X}_{EFH}$ from Belik et al. [22]:

$$T_{3',EFH} = T_{3'}\left(1 + \dot{X}_{EFH}\right) = T_{3'}\left(1 + \Lambda\Phi(1-\varepsilon)\right) \tag{5}$$

where Λ is the dimensionless heater length, Φ is the dimensionless heat source number, ε is the void fraction of the EFH material [22].

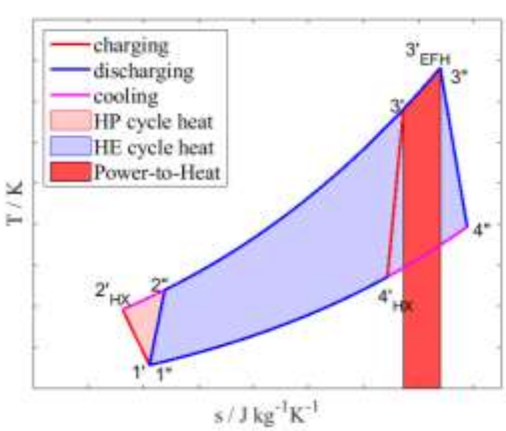

Fig. 2. T-s-diagram of Brayton heat pump (charging) and heat engine (discharging) cycles with electrical heat input (red area: 3’→3’$_{EFH}$) and applied turbomachines’ polytropic efficiency of $\eta_p = 0.90$

To calculate the discharged specific technical work w_t, the proportional relationship between specific enthalpy and temperature ($\Delta h_{HE} = \bar{c}_p\, \Delta T_{HE}$) given by the ideal gas law is applied assuming the averaged specific heat capacity of $\bar{c}_p = 1.14\ kJkg^{-1}K^{-1}$ for dry air at HT conditions of the ideal gas:

$$w_t = \bar{c}_p\, \Delta T_{HE} \tag{6}$$

where ΔT_{HE} is the total temperature difference provided by the HT- and LT-STES to run the Brayton heat engine cycle. Since a reversible heat transport from the storage inventory to the WF is assumed ($\eta_{STES} = 1$), we can express this temperature difference using turbomachine’s inlet and outlet temperatures:

$$\Delta T_{HE} = \Delta T_{turb''} - \Delta T_{comp''} = (T_{3''} - T_{4''}) - (T_{2''} - T_{1''}) \tag{7}$$

Substituting Eq. (7) in Eq. (6) with associated temperature definitions from Eq. (1) to (5) leads to an expression for w_t that is further simplified using the equivalent polytropic efficiency $\eta_p = \eta_{p,turb} = \eta_{p,comp}$ and equivalent thermal compression ratio $\Psi = \Psi_{turb} = \Psi_{comp}$ for the turbomachines:

$$w_t = \bar{c}_{p,F}\, \frac{\Psi^{-\eta_p}\left(T_{2',HX}\Psi^{\frac{-1}{\eta_p}} + T_{4',HX}(\dot{X}_{EFH}+1) - T_{2',HX}\right) + T_{4',HX}(\dot{X}_{EFH}+1)}{\Psi^{\frac{-1}{\eta_p}}} \tag{8}$$

Eq. (8) might be further specified using the definition $\Psi = \beta^{\frac{\kappa-1}{\kappa}}$ with the pressure ratio β and WF’s isentropic exponent κ:

$$w_{t,poly} = \bar{c}_{p,F}\, \frac{\left(\beta^{\frac{1-\kappa}{\kappa}}\right)^{\eta_p}\left(T_{2',HX}\left(\beta^{\frac{1-\kappa}{\kappa}}\right)^{1/\eta_p} + T_{4',HX}(\dot{X}_{EFH}+1) - T_{2',HX}\right) + T_{4',HX}(\dot{X}_{EFH}+1)}{\left(\beta^{\frac{1-\kappa}{\kappa}}\right)^{1/\eta_p}} \tag{9}$$

For $\eta_p = 1$ and $\dot{X}_{EFH} = 0$, Eqs. (8) and (9) reduce to a simplified expression that describes the isentropic process with ideal gas conditions:

$$w_{t,is} = \bar{c}_{p,F}\, T_{2',HX}\left(\beta^{\frac{1-\kappa}{\kappa}}\right) + \bar{c}_{p,F}\left(\beta^{\frac{\kappa-1}{\kappa}}\right) T_{4',HX} - 2\,\bar{c}_{p,F}\, T_{4',HX} + \bar{c}_{p,F}\left(T_{4',HX} - T_{2',HX}\right) \tag{10}$$

Results from Eq. (9) and (10) for dry air are presented in Fig. A1 from Appendix A for various pressure ratios and HX temperatures using averaged values for the specific heat capacity $\bar{c}_{p,air} = 1.14\ kJkg^{-1}K^{-1}$ and for the isentropic exponent $\kappa = 1.35$. These values have also been used to obtain results from Fig. 3.

The power ratio of the polytropic and isentropic process power output can be calculated using the ratio of the specific technical work from Eq. (9) and (10) with the associated mass flow rates:

$$\frac{P_{discharge,poly}}{P_{discharge,is}} = \frac{w_{t,poly}\, \dot{m}_{F,poly}}{w_{t,is}\, \dot{m}_{F,is}} = 1 \tag{11}$$

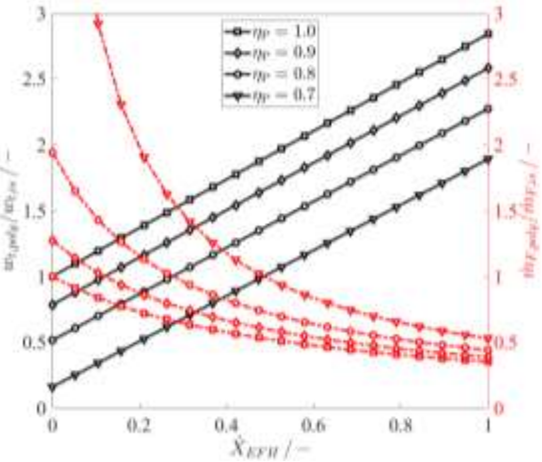

Fig. 3. Specific technical work and mass flow rate ratios for dry air: $\kappa = 1.35$, $\bar{c}_{p,air} = 1.14\ kJkg^{-1}K^{-1}$; $T_{4\prime,\mathrm{HX}} = [0:200]°C$; $T_{2\prime,\mathrm{HX}} = 20°C$: $\beta = [3:15]$

To analyze the impact of PtH integration we conducted a simulation study based on Eqs. (9) to (11) for WF air using various polytropic efficiencies η_P. The results presented in Fig. 3 confirm that an increasing electrically fed exergy rate $\dot{X}_{EFH}$ leads to a higher specific work output and thus to a lower mass flow rate during discharging. This effect is particularly evident at lower polytropic efficiency. In conclusion, the integration of PtH into the Brayton battery generally results in higher energy density and lower mass flow rates, which can be used to reduce the component size with associated cost reduction.

3 Modeling

A techno-economic analysis of the Brayton battery concept from Fig. 1 requires the interconnected modeling of the central components. The simulation algorithm is presented in Fig. 5, showing both the system-level and the component-level calculation procedures and the usage of the following governed equations.

In order to perform a detailed calculation on the system and component level, we obtained thermal properties from the CoolProp database [27] for heat capacity, density, thermal conductivity, and viscosity as a function of temperature at each cycle point in Fig. 2. We calculate entropy and enthalpy values in the same manner for the WF dry air, which is composed as a mixture of nitrogen, oxygen, and argon. In addition, water is used for HX as a heat-rejection fluid acquiring thermal properties from [27].

To ensure efficient computation, we used different model complexities on the component level according to component characteristics, as such components can be divided into static and transient. Regenerator-based STES and EFH have a transient behavior that requires detailed, multiple-dimension modeling. In contrast, a HX can be viewed as a stationary component, enabling a compact formula for mass and heat balance. As shown in Table 2, simplified formulations are suitable for modeling turbomachinery for which the isentropic state change is used to determine the outlet temperatures.

3.1 Turbomachines

Eqs. (1) to (4) are used to model compressors and turbines in a simplified fashion. In contrast to the analysis from section 2.2, real WF properties from [27] are used to determine the isentropic outlet temperatures $T_{F,out,is} = T_{F,in}\,\beta^{\frac{\kappa-1}{\kappa}}$ and enthalpies $h_{out,is}$. The isentropic efficiency η_{is} is then used to calculate the irreversible adiabatic compression outlet enthalpy

$$h_{out,comp} = \frac{h_{out,is} - h_{in}}{\eta_{is,comp}} + h_{in} \qquad (12)$$

and the irreversible adiabatic expansion outlet enthalpy

$$h_{out,turb} = \left(h_{out,is} - h_{in}\right) \cdot \eta_{is,turb} + h_{in} \qquad (13)$$

for both turbomachines.

The connected motor and generator are assumed to be permanent magnet synchronous machines with an exergetic efficiency of 97%.

3.2 Solid media thermal energy storage

3.2.1 Porous two-phase model

The counterflow STES has been investigated in the context of a Brayton battery in [19-23, 32, 33, 41]. The basis of these introduced models is Schumann's two-phase and one-dimensional model [42] with a time-varying temperature field during thermal cyclic operation. On this basis, a simplified thermal model can be formulated under three simplifying assumptions. First, the thermal storage capacity in the fluid phase is assumed to be small. Second, conduction is assumed to be exclusively axial due to the low thermal conductivity. Finally, thermal losses to the ambient are small for large-scale dimensions [30]. The one-dimensional axial model can be normalized in time t* and space z* and expressed as follows:

$$\frac{dT_S}{dt^*} = \Pi_{STES}(T_F - T_S) \qquad \text{with } \Pi_{STES} = \frac{k\,a_v\,\tau\,V_{STES}}{m_{STES}c_{p,STES}} \qquad (14)$$

$$\frac{\mathrm{dT_F}}{\mathrm{dz^*}} = \Lambda_{\mathrm{STES}}(\mathrm{T_S} - \mathrm{T_F}) \qquad \text{with } \Lambda_{STES} = \frac{k\,a_v\,V_{STES}}{\dot{m}_F c_{p,F}} \qquad (15)$$

The thermodynamic behavior can then be summarized with only the reduced period duration Π and the reduced regenerator length Λ_{STES}. Here, the solid and fluid phase temperatures are represented by T_S and T_F. Other properties of the setup are: a_v is the heat transfer surface to volume V_{STES} ratio, τ is the period duration, $\dot{m}_F$ is the mass flow rate, m_{STES} is the total STES inventory mass, and $c_{p,STES}$ and $c_{p,F}$ are the specific heat capacities of the fluid and the solid.

3.2.2 Packed bed regenerator

The characteristic parameters introduced in the previous section are set for the honeycomb inventory option using a reduced regenerator length of $\Lambda_{STES} = 100$, the specific surface area $a_v = 344\ \mathrm{m^{-1}}$ and a void fraction $\varepsilon = 0.70$ of a 10 m packed bed diameter. Pressure loss is considered for the design study and is limited to the practical value of 10 mbar using the correlation from [43]. These specifications have been chosen for both, the LT- and HT-STES, respectively. A temporal averaged fluid outlet temperature $T_{F,out}$ is used to simplify the modeling of the time-varying fluid outlet temperature on system-level simulation:

$$T_{F,out} = T_{F,in} - \eta_{ex,STES} \cdot \left(T_{in} - T_{in,cold}\right) \tag{16}$$

$$T_{F,out} = T_{F,in} + \eta_{ex,STES} \cdot \left(T_{in,hot} - T_{in}\right) \tag{17}$$

The outlet temperature is given by the cyclic inlet temperatures $T_{F,in}$ during charging and discharging period, as well as the regenerator's exergetic efficiency $\eta_{ex,STES}$:

$$\eta_{ex,STES} = \frac{|T_{F,in} - T_{F,out}|}{T_{F,hot,in} - T_{F,cold,in}} \tag{18}$$

3.3 Heat exchanger

3.3.1 NTU-ε-model

In order to describe the heat transfer in the HX, the well-known NTU-ε-model [44] has been applied with the assumption of small thermal losses. The efficiency of transferring heat from the air towards the water coolant during the charging period determines the thermal cyclic behavior of the HX. By considering the heat and mass balances, the hot and cold WF outlet temperatures can be determined using the HX effectiveness $\varepsilon_{\mathrm{HX}} = \dot{Q}_{HX}/\dot{Q}_{HX,max}$:

$$T_{F,hot,out} = -\varepsilon_{HX} \cdot \left(T_{F,hot,in} - T_{HX,in}\right) + T_{F,hot,in} \tag{19}$$

$$T_{F,cold,out} = \varepsilon_{HX} \cdot \left(T_{F,hot,in} - T_{HX,in}\right) + T_{HX,in} \tag{20}$$

Here, $T_{F,hot,in}$ and $T_{HX,in}$ represent the HX inlet temperatures of the hot WF and water coolant temperatures, where $T_{HX,in} = T_{2\prime,HX}$ for the first HX and $T_{HX,in} = T_{4\prime,HX}$ for the second HX. When the charging and discharging periods have equal durations and mass flow rates, only the heat exchanger effectiveness $\varepsilon_{\mathrm{HX}}$ is required. Finally, the heat exchanger size (NTU: number of transfer units) in counter flow is calculated as:

$$NTU = \frac{\varepsilon_{HX}}{1 - \varepsilon_{HX}} \tag{21}$$

This set of equations facilitates the computation of the pressurized air temperatures and water coolant after passing through the heat exchanger during the cyclic Brayton CB operation.

3.3.2 Shell-and-tube heat exchanger

Shell-and-tube heat exchangers are considered using the *ε-NTU* in combination with the Kern method [44], applying the operating conditions of the Brayton battery. The heat transfer tubes have a set length of $L_{HX} = 9$ m, a thickness of 2 mm and an outer tube diameter of 38 mm. To reduce pressure loss, the WF flows through the shell side, which is fixed at a pressure loss of 20 mbar. The design method is described in detail in [44].

3.4 Electric flow heater

3.4.1 Porous two-phase model with heat source

The modeling approach for the EFH is based on a simplified two-phase transient model developed by Belik et al. [22]. This approach uses dimensionless characteristic parameters referred to as heat source number Φ, heater length Λ_{EFH}, heater loss number Γ_{EFH} and Stanton number St. The one-dimensional axial model is normalized in time t^* for the solid phase (S)

$$\frac{dT_S}{dt^*} = \Phi\, St\, T_{F,in} + \frac{St}{1-\varepsilon}\left(T_F - T_S\right) \tag{22}$$

and in space z^* for the fluid phase (F)

$$\frac{dT_F}{dz^*} = \Lambda_{EFH}\left(T_S - T_F\right) - \Gamma_{EFH}\left(T_F - T_0\right) \tag{23}$$

using the Dirichlet boundary condition for the inlet $T_{F,in} = T_{3\prime}$ and adiabatic boundary condition for the outlet $-\lambda \frac{\partial T_{S,F}}{\partial z^*} = 0$.

The introduced formulation describes the thermodynamic behavior of the EFH with only four dimensionless parameters. Neglecting thermal insulation losses to the ambient with $\Gamma_{EFH} = 0$, this formulation reduces to only three parameters:

$$\Phi = \frac{\dot{Q}_{PtH}}{V_{EFH}(1-\varepsilon)\, k\, a_v\, T_{F,in}} = \frac{\dot{q}_{PtH}}{k\, a_v\, T_{F,in}} \tag{24}$$

$$\Lambda_{EFH} = \frac{k\, a_v\, H_{EFH}}{w_F\, \varepsilon\, \bar{\rho}_F\, \bar{c}_{p,F}} \tag{25}$$

$$St = \frac{k\, a_v\, \tau}{\bar{\rho}_{EFH}\, \bar{c}_{p,EFH}} \tag{26}$$

where $\dot{Q}_{PtH}$ represents the electrical heat source inside the total EFH volume, V_{EFH}, k denotes the heat transfer coefficient to the porous media, and a_v the surface area-to-volume ratio for the convective heat transfer. Furthermore, H_{EFH} gives the length, w_F represents the fluid's velocity, $\bar{\rho}_{EFH}$ denotes the solid's density, $\bar{c}_{p,EFH}$ gives the solid's heat capacity, and τ' indicates the charging duration.

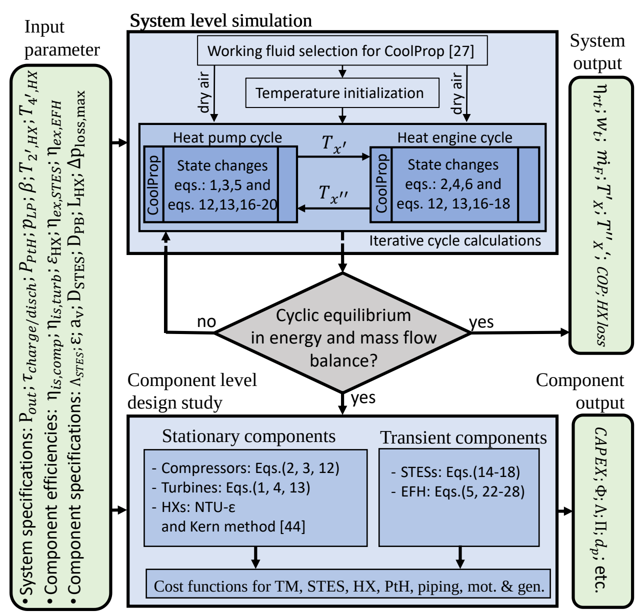

Fig. 4. Simulation algorithm for system and component level calculations

3.4.2 *Induction air heater*

The introduced general modeling approach can be adjusted to the proposed EFH concept, referred to as the induction air heater. This EFH concept achieves high process temperatures due to the typically high power density of the induction heating technology [45] required for the application in Brayton CB. A dispersed silicon infiltrated silicon carbide (SiSiC) pebble bed (PB) is proposed to obtain a high heater efficiency of 85% [40], even at the required heater temperatures beyond the Curie point of steel (768 °C). This PB has a typical void fraction of $\varepsilon = 0.40$, a specific averaged heat capacity of $\bar{c}_{p,SiSiC} = 1.10\ kJ\ kg^{-1}K^{-1}$, and an averaged material density of $\bar{\rho}_{SiSiC} = 2800\ kg\ m^{-3}$.

The following formulation for the heat source term $\dot{Q}_{PtH}$ is taken from [40] where the volumetric power density $\dot{q}_{ind,PB}$ is generated inside the inductively heated pebble bed volume V_{PB}:

$$\dot{Q}_{PtH} = \dot{q}_{ind,PB} V_{PB} \tag{27}$$

The volumetric power density is given as:

$$\dot{q}_{ind,PB} = 0.75 H_o^2 2\pi f \mu_0 F \tag{28}$$

where H_0 is the external magnetic field strength, f is the frequency, μ_0 is the magnetic field constant, and F is the power transmission factor defined in [40], that characterizes the effectiveness of energy dissipation inside the pebble bed. The volume of the pebble bed is finally given by

$$V_{PB} = \frac{\pi}{4} D_{PB}^2 H_{PB} (1 - \varepsilon) \tag{29}$$

using the outer diameter, which is fixed to $D_{PB} = 1.5\ m$ and the variable bed height that corresponds for the design study to the heater length $H_{PB} = H_{EFH}$. The pressure drop of the pebble bed is calculated using the formulation given by Ergun [46].

4 Simulation setup

The governed equations from Section 3 are implemented into the Matlab environment based on the procedure from Fig. 5 using Eqs. (14) and (15), as well as Eqs. (22) and (23), the system can be numerically solved by using a backward finite-difference method in space. The WF temperatures are obtained from [27] at each iteration and in each cycle point until reaching the cyclic equilibrium, as shown in Fig. 4. This convergence criterion is satisfied once the difference between temperatures is below 10^{-6} K. On a component level, several cycles of operation must be computed to obtain the thermal equilibrium condition inside both STES components. Here, the simulation ends when the change in thermal energy falls below 10^{-4} J in between cycles.

5 Results of parametric studies

In this study, an investigation of a Brayton CB system was conducted under a steady-state operating condition with a 7 h charging period and a 7 h discharging period. The total storage capacity of the investigated system is 210 MWh.

To quantify the potential of leveraging the system costs and the influence on RTE through additional PtH integration, parameter studies are conducted. For this purpose, we applied the component models and their specifications introduced in chapter 3 using the simulation algorithm from Fig. 4. In doing so, we considered pressure drops for STESs, EFH, and HXs, but neglected their thermal losses.

In section 5.1 we first conduct a brief techno-economic analysis to obtain a technical indicator for system's capital expenditures (CAPEX). The found correlation is then used in further sections for cost reasoning. In section 5.2, we present a sensitivity analysis results for a system without the EFH component in order to evaluate the influence of turbomachinery, HXs and STESs on the RTE η_{rt}. Then we integrated the EFH to investigate its impact on system cost and RTE. we carried out a design study for the EFH component to provide design solutions for HT application in a Brayton CB.

5.1 *Correlation to system costs*

In order to identify a technical key performance indicator that correlates with the CAPEX, simulation studies are conducted applying component models introduced in chapter 3 together with cost functions from Peters et al. [44] (HX and piping) and from the ADELE-ING project [11, 12] (TM, STES and EFH). In this study, the 210 MWh Brayton battery system with efficient STES regenerator solutions ($\eta_{ex,STES} = 0.95$) has been investigated varying the pressure ratio β and the HX4 efficiency in the range $\varepsilon_{\mathrm{HX4}} = [0.50{:}\,0.90]$ similar to the study from section 5.3. In addition to this parameter variation, electrical heating with up to 35 MW ($\dot{X}_{EFH} = 0.23$) is applied to the system to compare the discharged specific technical work w_t with the CAPEX C_{CAPEX}. The total CAPEX is the sum of all component costs that is multiplied by two factors f_{i} and f_{c}, which consider installation and contingency costs, respectively: $C_{CAPEX} = f_i f_c \sum C_i$. Both factors are assumed to be 1.1 that is the average value taken from [44].

Results from Fig. 5 demonstrate a correlation between the specific technical work and the CAPEX for various pressure ratios and the both cases, with additional electrical heating (left) and without it (right). Accordingly, the CAPEX can be estimated as inversely proportional to the root of the specific technical work by the following relation:

$$C_{CAPEX} \sim w_t^{-0.5}$$

The linear regression fit with a high coefficient of determination of $R^2 = 0.9739$ proves the linearity and returns the coefficient of proportionality $p = 3100\ €\sqrt{Wh}/kWh/\sqrt{kg_{air}}$ and $c = -35.6\ €/kWh$ to express the following linear relationship

$$\tilde{C}_{CAPEX} = 3100\, w_t^{-0.5} - 35.6\ \forall\ w_t^{-0.5} \in [0.09{,}0.3] kg^{0.5} Wh^{-0.5} \tag{30}$$

that can be expressed in [€/Wh] using $p = 3.10\ €/\sqrt{Wh \cdot kg_{air}}$:

$$\tilde{C}_{CAPEX} = 3.1\, w_t^{-0.5} - 0.0356\ \forall\ w_t^{-0.5} \in [0.09{,}0.3] kg^{0.5} Wh^{-0.5} \tag{31}$$

This found correlation is in particular valid for an operation under ideal gas conditions with temperatures far beyond 500 °C and pressure ratios above 9. Especially in the validity range of $0.09\ kg^{0.5}Wh^{-0.5} < w_t^{-0.5} < 0.18\ kg^{0.5}Wh^{-0.5}$, a minor variation of the results is observed. In conclusion, this revealed

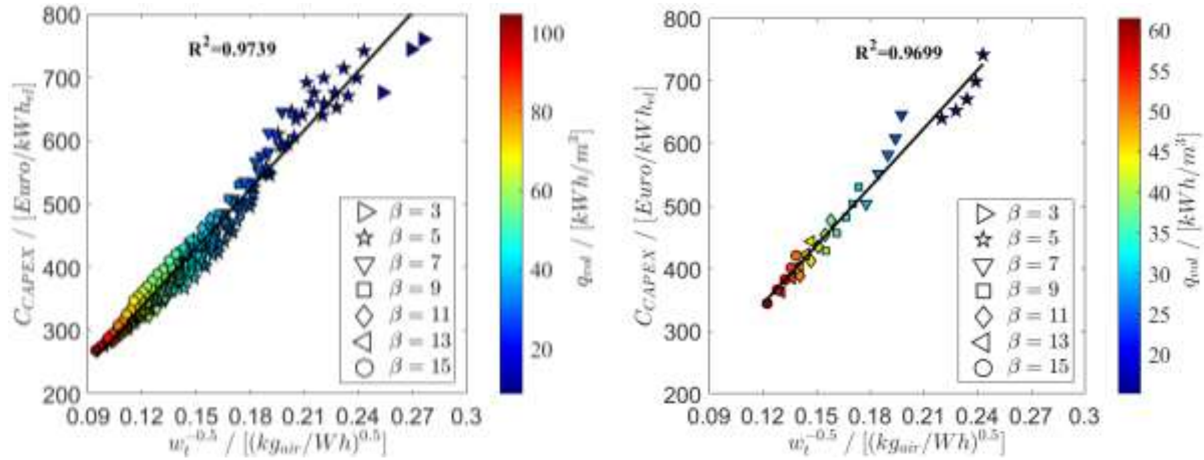

Fig. 5. Correlation between system cost and specific technical work valid for $\beta = [3{:}15]$ *and* $w_t^{-0.5} = [0.09{:}0.30]$; left: case with additional electrical heating; and right: case without electrical heating

relationship indicates the system costs with only two derived indicators: The mass of the working fluid m_{WF} cyclically circulated in the system and the technical work w_t delivered by the system. We use only the technical work as an indicator for further cost reasoning in this work.

Furthermore, the comparison of the volumetric energy density (color coded) between both cases from Fig. 5 shows the maximum increase by 70% to 104.6 kWh/m^3 for the case with added electrical heating and $\beta = 15$. In comparison, Benato's techno-economic assessment for a TES build-up with Al_2O_3 bricks demonstrated an energy density increase by 105% to 430 kWh/m^3 accompanied by a CAPEX reduction of 35% to 54 $/kWh using low-cost turbomachinery. Chen et al. [21] also achieved a redoubling of the energy density to 62.2 kWh/m^3 by adding electrical heating into the proposed hybrid system.

Table 3. Component efficiencies defined for parameter study

$\eta_{is,turb}$	$\eta_{is,comp}$	$\eta_{ex,STES}$	ε_{HX2}	ε_{HX4}	η_{EFH}	$\eta_{M/G}$
0.90	0.87	0.85-0.95	0.90	0.5-0.90	0.85	0.97

5.2 *Sensitivity analysis*

To investigate the influence of each component on RTE and CAPEX, we conducted a sensitivity analysis, taking into account the set of central specifications listed in Table 3. In addition, the efficiencies of the following components were varied for this purpose: exergetic efficiencies $\eta_{ex,STES}$ of both STESs, effectivenesses $\varepsilon_{\mathrm{HX}}$ of both HXs and isentropic efficiencies η_{is} of turbomachines. All these parameters are indicated in Fig. 6 with the notation "η_{i}."

The results from Fig. 6 without PtH implementation are presented at the design point $\eta_i = 0.90$, with an RTE of 48% and capital costs per unit energy discharged of 384 €/kWh$_{el}$. As expected, increasing component efficiency leads to an increased RTE.

Table 4. Central specifications for system level simulations

Working fluid	$T_{4',Comp,in} = T_{4',HX}$	$T_{2',HX}$	p_{LP}	β
Air (real gas)	245 °C	20 °C	1 bar	10

The turbomachines have a dominant impact on the efficiency here. In particular, the turbines show the greatest impact on that performance metric since their exhaust loss at $T_{4''}$ (see Fig. 2) is associated with the highest exergy loss. In contrast, HXs have a marginal impact on RTE, however, the specific costs significantly increase with an increasing HX effectiveness due to the enormously rising heat transfer area. Moreover, this study shows that both STESs have significant impact on the RTE as well as on the specific system costs, since these components improve the energy density of the system by providing exergy enriched high-temperature heat to the Brayton HE cycle with high efficiencies. Therefore, to achieve a high cost efficiency and a high energy efficiency, STES components must have high efficiencies above 90%.

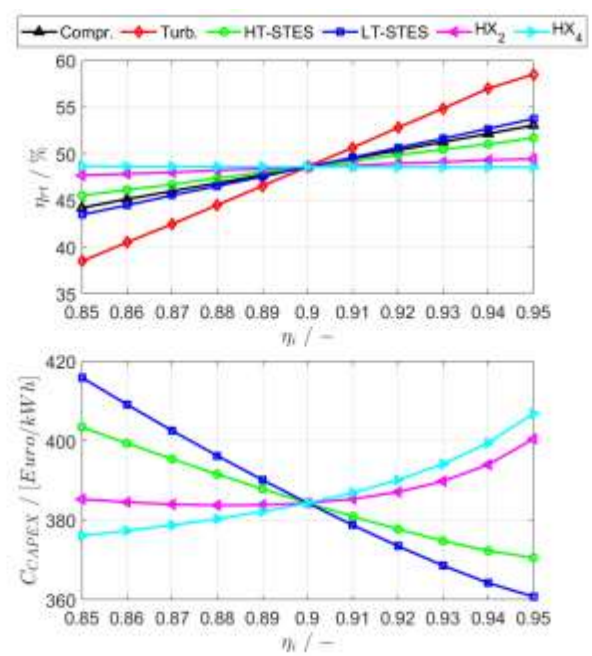

Fig. 6. RTE and specific CAPEX of a 210 MWh, 600°C Brayton CB system without EFH for efficiencies $\eta_i = [0.85{:}0.95]$

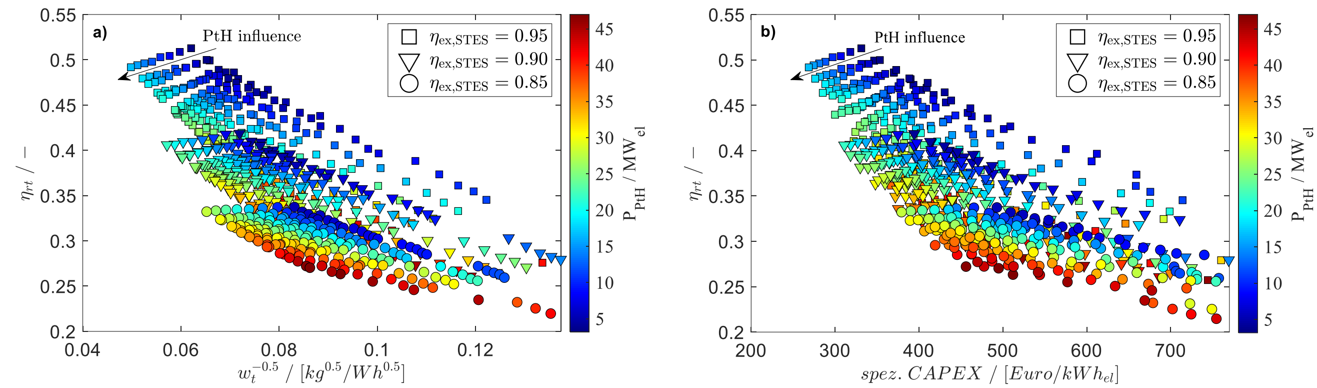

Fig. 7. Brayton CB design solutions for RTE and spec. technical work a) and spec. CAPEX b) in relation to the electric heating power

5.3 *Parameter study*

In contrast to the sensitivity analysis, where component efficiencies varied and process parameters remained, as presented in Table 3, this study aims to vary process parameters as HX temperatures, pressure ratios and electric heating power at fixed efficiencies. The component efficiencies indicated in Table 4 have been chosen on the basis of the findings from the previous section, which indicate that turbomachines and STES components have high efficiencies while HX and EFH have lower efficiencies in order to save costs and thus achieve higher cost efficiency. Aside from the variation of the heating rate, the pressure ratio β has been varied from 3 to 15 whereby the effectiveness ε_{HX4} of HX4 and STES efficiency have been varied from 0.50 to 0.90 and from 0.85 to 0.95, respectively. The HX temperatures have been set to 20°C for the HX2 in the high-pressure stage and to 100°C for the HX4 in the low-pressure stage. The induction air heater is assumed to operate with an induction air heater efficiency of 85%, which agrees with the study from [40] at laboratory scale for outlet temperatures up to 700°C.

Fig. 7 presents a variety of Brayton battery design solutions based on the wide-ranged parameter study comparing the RTE to the square root of the inverse technical work a) and to the specific CAPEX b). The comparison between the design solutions from Fig 7 a) and b) clearly shows the linear relationship found in section 5.1, in particular for design solutions with a high STES efficiency of 95%.

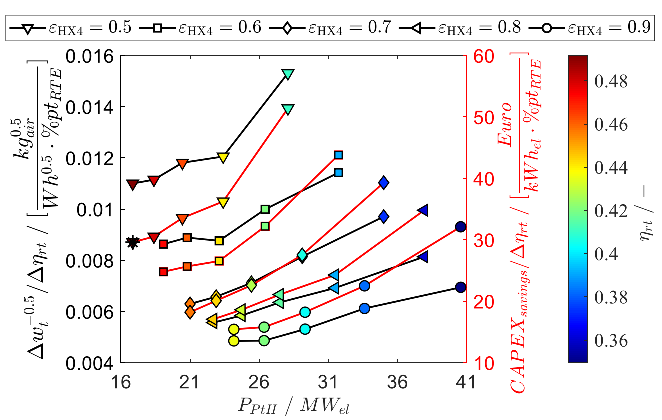

Fig. 8. Cost reduction potential through additional electric heating power on design solutions from Fig. 7 for $\eta_{ex,STES} = 0.95$ and for various ε_{HX4}

The electric heating power is color coded and shows its influence on RTE and CAPEX: higher heating rates result in reduced system costs but also in lower RTE. The effect of cost reduction to the detriment of efficiency has already been presented in [19] for A-CAES and in [21] for a hybrid storage system comprising a HT-PTES with an ORC cycle.

To highlight the influence of the EFH on system costs and RTE, and to quantify the tradeoff between these both investment criteria, we further analyzed in Fig. 8 the difference quotients with respect to electric heating power. To this end, we extracted part of the results from Fig. 7 for $\eta_{ex,STES} = 0.95$ and calculated the difference quotients for specific technical work $\Delta w_t^{-0.5}/\Delta\eta_{rt}$ and for the CAPEX $\Delta CAPEX/\Delta\eta_{rt}$ with respect to the absolute RTE loss of 1% point.

The results quantify the effect of cost reduction, caused by the additional electric heating power. The difference quotient for cost savings increases with less effective HX designs from 15 €/kWh/%pt$_{RTE}$ to almost 60 €/kWh/%pt$_{RTE}$. The reduced HX effectiveness lifts the inlet temperature of the HP compressor and improves the coefficient of performance (COP) for the HP cycle. The higher COP leads to improved energy-efficiency which is illustrated by the color-coded RTE in Fig. 8. As a result, the efficiency losses caused by the electrical heating are limited in relation to the total loss of RTE, hence the cost reduction effect of the EFH increases. This effect is amplified if the heating takes place at high temperatures, as this minimizes energy losses of the EFH. The tradeoff between CAPEX and RTE is further illustrated in Fig. 9 by extracting the solution marked with '*' from Fig. 8 at 30 €/kWh cost savings per 1 %pt of RTE. Results from Fig. 9 clearly demonstrate the CAPEX reduction for all system components besides the EFH itself. As a result, an electric heating power of 17 MW reduce the system CAPEX to less than 300 €/kWh$_{el}$. In addition, the applicability of the cost estimation function from Eq. (30) is demonstrated in Fig. 9: The linear $\tilde{C}_{CAPEX}$function illustrated by the dashed line, underestimates the sum of the equipment costs C_{CAPEX} by a maximum of 7%. Moreover, the red line depicted in Fig. 9 shows the RTE, which likewise decreases, but with a reduced slope: While the efficiency loss is only 5%, the costs are reduced by 23% compared to the case without PtH integration (360 €/kWh; $\eta_{rt} = 0.517$). Overall, according to the results from this parameter study, CAPEX are significantly reduced with an increased heating power. Furthermore, this cost reduction effect offers the plant operator the flexibility to adjust CAPEX by the installed EFH capacity.

The results presented in Fig. 7 and Fig. 9 have been additionally verified using cost functions from [18]. Additional information regarding the verification approach and results for the highest STES efficiency of 95% can be found in Appendix B. Fig. B1 shows similar results compared with the outcomes reported in Fig. 7 b) and therefore leads to identical conclusions. However, there are major differences to our results in the distribution of system costs, which are illustrated in Fig. B2. While our results identified the turbomachinery as the major expense, Benato's cost distribution shows that the highest costs are associated with the thermal energy storage components. In addition, Benato's cost expressions for motor and generator units have only a minor impact on the total cost of the Brayton CB. In contrast, the electric heating component significantly influence the system CAPEX: while Benato's expression gives electric flow heater cost of up to 850 €/kW$_{el}$, we obtained 160 €/kW$_{el}$ for the utility scale induction air heater. Even if we apply Benato's formulation for the electric heater cost ($C_{\mathrm{EFH}} = 75000 \cdot P_{EFH}^{0.9}$), a slight reduction of system CAPEX still occurs, confirming our main conclusion on cost leverage. However, this cost reduction effect dissipates at marginal cost of around 950 €/kW$_{el}$ resulting in reduced cost efficiency and energy efficiency as well.

5.4 *Induction air heater design solutions*

Induction heating has the potential to convert utility-scale electric power into high-temperature (HT) heat. However, a sufficiently high heat transfer area must be provided to transfer the induced HT heat to the gaseous WF. Therefore, the objective of this design study is on the one hand, to calculate the heat transfer area of the proposed pebble bed air heater PtH concept, and on the other hand, to determine its dimensions. To this end, we chose results with the highest RTE from section 5.2 to obtain design solutions for the EFH using the design tool formulated in section 3.4 and material specifications for silicon carbide obtained from [40]. To allow a proper comparison of the design solutions, the component's pressure loss is set to 100 mbar. Moreover, the induction air

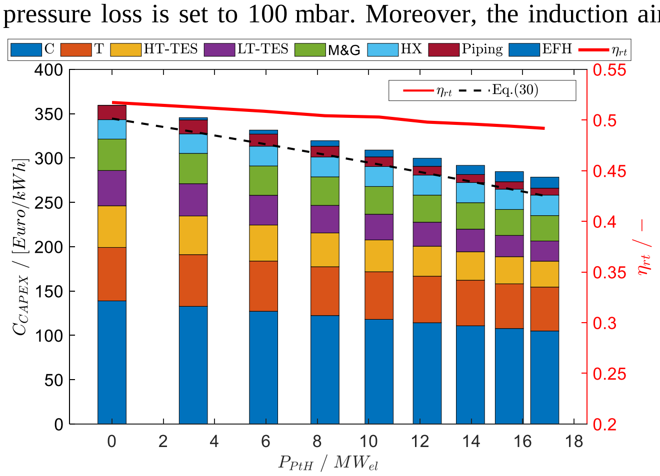

Fig. 9. Cost reduction effect through additional heating power on design configuration '*' from Fig. 8: $\beta = 15$, $\varepsilon_{\mathrm{HX4}} = 0.50$, $T_{2,\mathrm{HX}} = 20\,°C$, $\eta_{\mathrm{ex,STES}} = 0.95$; and demonstration of CAPEX estimation using Eq. (30)

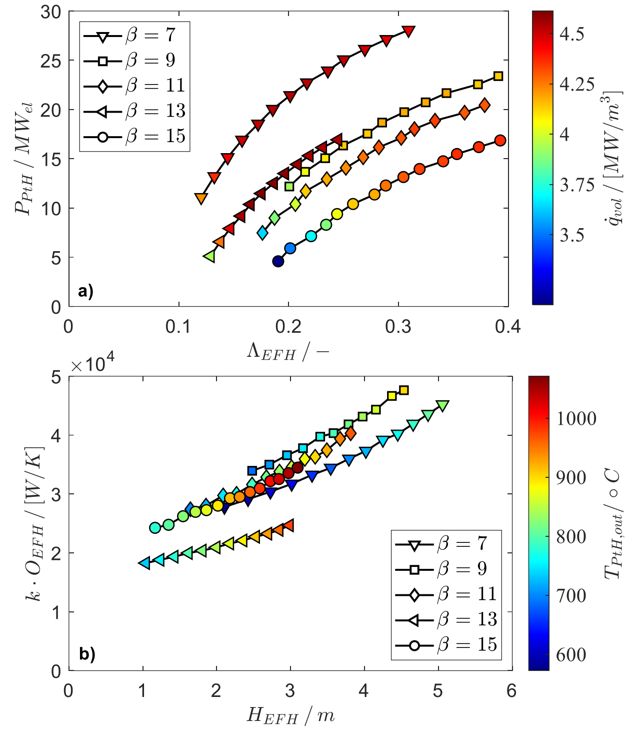

Fig. 10. EFH design solutions with three pressure vessels, each with D_{PB} = 1.5 m, η_{PtH} = 0.85: a) electric heating power related to dimensionless parameters from sec. 3.4.1; b) $k{*}O$ in relation to the required heater length H_{EFH}

heater operates at 85% efficiency using a frequency of 5 kHz and a peak current in the inductor windings of 800 A.

Fig. 10 presents design solutions for the induction air heater in a dimensionless manner a) using the dimensionless heater length Λ_{EFH}, and in a dimensioned way b), giving the outlet temperature in relation to the EFH bed height. Both diagrams show that to achieve a high volumetric power density $\dot{q}_{vol}$ together with a high outlet temperature $T_{PtH,out}$, either the heat transfer surface O_{EFH} or the heat transfer coefficient k must increase with a larger heater length (i.e., larger PB height). Moreover, to ensure a given pressure loss of 100 mbar for the obtained bed height, an EFH configuration with three modules is needed where corresponding sphere diameters between 120 mm and 180 mm are used. Thus, bed heights of up to 5 m in each module are required to ensure maximum temperatures of up to 1050 °C with a volumetric power density below 4.5 MW/m^3. Such high temperatures can be achieved by available resistive EFH only at the expense of its operational lifetime. Therefore, the silicon-carbide-based induction heater is an affordable and feasible solution that meets the high-temperature requirements of a Brayton CB application ensuring high lifetime expectations.

6 Conclusions

A techno-economic study has been conducted to assess the impact of additional Power-to-Heat (PtH) integration on a closed-loop Brayton Carnot battery (CB) system. The objective of this study was to quantify the tradeoff between system cost and round-trip efficiency (RTE) arising from the integration of the additional electric heating and to provide novel design solutions for such a high-temperature electric heating (HT-EH) component. To this end, component models for the central components were developed and implemented in the system model together with associated cost functions. On this modeling basis, we investigated a Brayton CB air system with 210 MWh energy storage capacity and a seven-hour charging and discharging periods under a cyclic steady-state operating condition and evaluated the influence of additional electric heating rates on cost and energy efficiency.

The primary results of this contribution are as follows:

- A correlation was found between system costs C_{CAPEX} and discharged specific technical work w_t ($C_{CAPEX} \sim w_t^{-0.5}$) to estimate cost reduction due to additional electrical heating
- This correlation reveals that CAPEX are principally affected by the working fluid's mass cyclically circulated in the system and by its delivered technical work
- The linear cost function derived demonstrates the significant decline in CAPEX with increasing technical work, which can be increased by additional electric heating
- A sensitivity analysis of component efficiencies clarifies that the turbomachinery primarily and the solid media thermal energy storages secondarily must have efficiencies above 90% to ensure high cost efficiency and high energy efficiency as well for the system
- The parameter study proves that additional integration of an HT electric flow heater (EFH) upstream of the HT-STES is a cost-effective way to increase the specific technical work and thus reduce the cost of the Brayton CB. However, with the penalty of reduced round-trip efficiency, an additional electric heating power of up to 17 MW results in a cost reduction of up to 23% to < 300 €/kWh, along with an efficiency loss below 5% to 49% RTE.
- The design study for an induction air heater based on an inductively heated silicon infiltrated silicon carbide pebble bed reveals a compact container design providing an outlet temperature of 1050 °C with a power density of 4.5 MW/m^3

Altogether, PtH integration offers a significant cost leverage for the Brayton CB when a compact EFH is added into the system. However, this novel component must provide high outlet temperatures above 1000 °C under pressures above 10 bar while maintaining a high conversion efficiency of over 85%. Since parasitic losses of induction heating and thermal losses to the ambient have been neglected in this work, further research effort needs to be carried out to propose design solutions for the insulated pressure vessel and to validate this PtH concept under the HT working conditions of the Brayton Carnot battery.

APPENDIX A

To illustrate the major impact of pressure ratio β and HX temperature (i.e. HP compressor inlet temperature) on the specific technical work w_t, the results of Eq. (9) and (10) for dry air are presented in Fig. A1. The results show a linear increase in the specific technical work for both process parameters. In addition, the results illustrate the difference between the polytropic process and an ideal isentropic process.

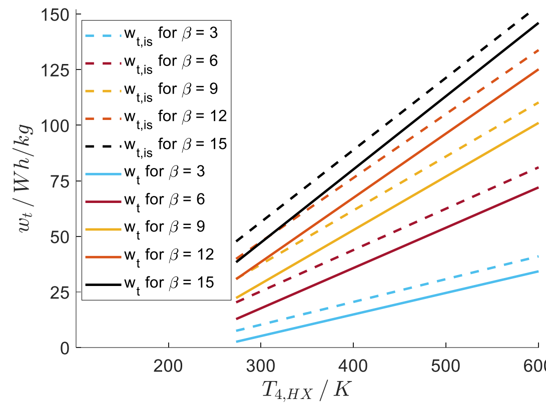

Fig. A1 Comparison of polytropic (at $\eta_p = 0.9$) and isentropic (at $\eta_p = 1.0$) specific technical work results based on the thermodynamic analysis from section 2.2 using $\bar{c}_{p,air} = 1.14\ kJkg^{-1}K^{-1}$ and $\kappa = 1.35$.

APPENDIX B

To verify that our results are robustness to the use of different cost functions, we recalculated our design solutions from Fig. 7 b) using cost expressions from Benato [18]. In addition to cost functions taken from [18], we applied our piping cost to calculate the total capital cost, which equal the sum of all component CAPEX. This value is further multiplied by Benato's system cost factor and currency exchange rate €/$ of 1.12.

The results of this robustness check are presented in Fig. B1 for a thermal energy storage efficiency of $\eta_{ex,STES} = 0.95$. Fig. B1 illustrates results that are similar to the main findings reported in Fig. 7 b), which lead to identical conclusions of cost reduction through increased additional heating power.

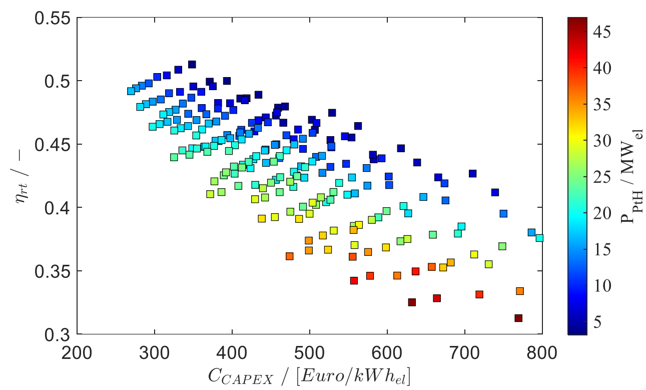

Fig. B1 Techno-economic assessment using Benato's [18] cost functions for a comparison to results for efficient STES designs with $\eta_{ex,STES} = 0.95$ from Fig. 7 b).

Moreover, Fig. B2 presents the distribution of system CAPEX for design solutions from Fig. 9 using Benato's cost functions. Although the electric heating component has significantly higher costs, the results confirm the cost reduction effect. However, this effect vanishes at the marginal cost of around 950 €/kW resulting in higher system costs and lower RTE.

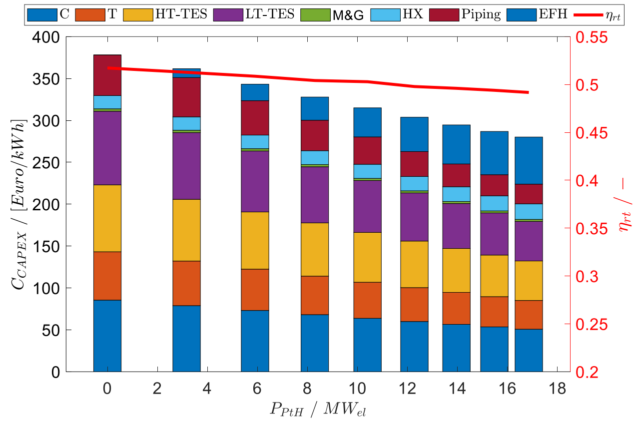

Fig. B2 Cost reduction through additional electric heating power for design solutions from Fig. 9 using Benato's [18] cost functions. (C: compressors; T: turbines; TES: thermal energy storages; M&G: motor and generator; HX: heat exchanger; EFH: electric flow heater)

References

[1] Renewable Energy Policy Network for the 21st Century, Renewables 2022 Global Status Report, REN21, 2022. www.ren21.net/wp-content/uploads/2019/05/GSR2022_Full_Report.pdf

[2] Rehman, S., Al-Hadhrami, L.M., Alam, M.M.. Pumped hydro energy storage system: a technological review. Renewable and Sustainable Energy Reviews 2015;44:586–598. doi:10.1016/j.rser.2014.12.040

[3] Barbour, E.,Wilson, I.G., Radcliffe, J., Ding, Y., Li, Y.. A review of pumped hydro energy storage development in significant international electricity markets. Renewable and Sustainable Energy Reviews 2016;61:421– 432. doi:10.1016/j.rser.2016.04.019.

[4] Budt, M., Wolf, D., Span, R., Yan, J.. A review on compressed air energy storage: Basic principles, past milestones and recent developments. Applied Energy 2016;170:250–268. doi:10.1016/j.apenergy.2016.02.108.

[5] A. Benato, A. Stoppato, Pumped Thermal Electricity Storage: a technology overview, Thermal Science and Engineering Progress (2018), doi: https://doi.org/10.1016/j.tsep.2018.01.017

[6] Dumont, Olivier, et al. "Carnot battery technology: A state-of-the-art review." Journal of Energy Storage 32 (2020): 101756.

[7] Liang, Ting, et al. "Key components for Carnot Battery: Technology review, technical barriers and selection criteria." *Renewable and Sustainable Energy Reviews* 163 (2022): 112478.

[8] Vecchi, Andrea, et al. "Carnot Battery development: A review on system performance, applications and commercial state-of-the-art." *Journal of Energy Storage* 55 (2022): 105782.

[9] De Sisternes, F. J., Jenkins, J. D., and Botterud, A., 2016, "The Value of Energy Storage in Decarbonizing the Electricity Sector," Applied Energy, 175, pp. 368–379.

[10] Xue, Haobai. A comparative analysis and optimisation of thermo-mechanical energy storage technologies. Diss. University of Cambridge, 2019.

[11] S. Zunft, V. Dreissigacker, M. Bieber, A. Banach, C. Klabunde and O. Warweg, "Electricity storage with adiabatic compressed air energy storage: Results of the BMWi-project ADELE-ING," in *Proc. 2017 International ETG Congress*, Bonn, Germany, pp. 1-5.

[12] Zunft, S., Krüger, M., Dreißigacker, V., Belik, S., Hahn, J., & Knödler, P. (2017). *ADELE-ING: Engineering-Vorhaben für die Errichtung der ersten Demonstrationsanlage zur adiabaten Druckluftspeichertechnik: official report*. Ed. Züblin AG. Stuttgart

[13] Mercangöz, M., Hemrle, J., Kaufmann, L., Z'Graggen, A., & Ohler, C. (2012). Electrothermal energy storage with transcritical CO2 cycles. Energy, 45(1), 407-415.https://doi.org/10.1016/j.energy.2012.03.013

[14] MAN, Energy Storage. "Electro-thermal energy storage", https://www.man-es.com/energy-storage/solutions/energy-storage/electro-thermal-energy-storage; 2021 [accessed 3 January 2023]

[15] Steinmann, W. D. (2014). The CHEST (Compressed Heat Energy STorage) concept for facility scale thermo mechanical energy storage. Energy, 69, 543-552. doi: https://doi.org/10.1016/j.energy.2014.03.049

[16] SIEMENS, "Siemens presents thermal storage solution for wind energy", 27 September 2016 (2016-09-27), WindEnergy Hamburg Ref nr: PR2016090419WPEN, pages 1 - 4, XP055456571; 2021 [accessed 03 January 2023]

[17] Trieb, Franz, and André Thess. "Storage plants–a solution to the residual load challenge of the power sector?." *Journal of Energy Storage* 31

[18] Benato, A.. Performance and cost evaluation of an innovative pumped thermal electricity storage power system. Energy 2017;138:419–436. doi:10.1016/j.energy.2017.07.066.

[19] Dreißigacker, Volker, and Sergej Belik. "System Configurations and Operational Concepts for Highly Efficient Utilization of Power-to-Heat in A-CAES." Applied Sciences 9.7 (2019): 1317.

[20] Houssainy, S., Janbozorgi, M., & Kavehpour, P. (2018). Thermodynamic performance and cost optimization of a novel hybrid thermal-compressed air energy storage system design. *Journal of Energy Storage*, *18*, 206-217. https://doi.org/10.1016/j.est.2018.05.004

[21] Chen, L. X., Hu, P., Zhao, P. P., Xie, M. N., & Wang, F. X. (2018). Thermodynamic analysis of a high temperature pumped thermal electricity storage (HT-PTES) integrated with a parallel organic Rankine cycle (ORC). *Energy Conversion and Management*, *177*, 150-160.

[22] Belik, Sergej, Volker Dreissigacker, and Stefan Zunft. "Power-to-heat integration in regenerator storage: Enhancing thermal storage capacity and performance." Journal of Energy Storage 50 (2022): 104570.

[23] Desrues, T., Ruer, J., Marty, P., Fourmigué, J.. A thermal energy storage process for large scale electric applications. Applied Thermal Engineering

[24] Silvia T., Bjarke B. Rafael G.: "Techno-Economic Assessment of a Carnot Battery for Industrial Application." In: 3rd International Workshop of Carnot Batteries. (IWCB), Stuttgart, Germany; September 2022.

[25] Steinmann, W. D., Jockenhöfer, H., & Bauer, D. (2020). Thermodynamic analysis of high-temperature carnot battery concepts. *Energy Technology*, *8*(3), 1900895. https://doi.org/10.1002/ente.201900895

[26] Zhao, Y., Song, J., Liu, M., Zhao, Y., Olympios, A. V., Sapin, P., ... & Markides, C. N. (2022). Thermo-economic assessments of pumped-thermal electricity storage systems employing sensible heat storage materials. *Renewable Energy*, *186*, 431-456.

[27] Bell IH, Wronski J, Quoilin S, Lemort V. Pure and Pseudo-pure Fluid Thermophysical Property Evaluation and the Open-Source Thermophysical Property Library CoolProp. Ind Eng Chem Res. 2014 Feb 12;53(6):2498-2508. doi: 10.1021/ie4033999.

[28] NIST Standard Reference Database 23. NIST thermodynamic and transport properties of refrigerants and refrigerant mixture REFPROP, version 9.1; 2013.

[29] McTigue, Joshua D., et al. "Techno-economic analysis of recuperated Joule-Brayton pumped thermal energy storage." *Energy Conversion and Management* 252 (2022): 115016.

[30] Hausen, H. *Wärmeübertragung im Gegenstrom, Gleichstrom und Kreuzstrom.* Springer, Berlin, Heidelberg, 1976.

[31] Shah, K.R.; Sekulic, D.P. Fundamentals of Heat Exchanger Design; John Wiley & Sons: Hoboken, NJ, USA, 2003; ISBN 0-471-32171-0.

[32] Singh, R., Saini, R. P., & Saini, J. S. (2008). Simulated performance of packed bed solar energy storage system having storage material elements of large size-Part I. *The Open Fuels & Energy Science Journal*, *1*(1).

[33] Benato, A., Stoppato, A.. Energy and cost analysis of a new packed bed pumped thermal electricity unit. Journal of Energy Resources Technology 2018;140(2):020904. doi:10.1115/1.4038197.

[34] Zhang, H., Wang, L., Lin, X., & Chen, H. (2023). Parametric optimisation and thermo-economic analysis of Joule–Brayton cycle-based pumped thermal electricity storage system under various charging–discharging periods. Energy, 263, 125908.

[35] M. Abarr, B. Geels, J. Hertzberg, L.D. Montoya Pumped thermal energy storage and bottoming system part A: concept and model Energy (2016), pp. 1-12, 10.1016/j.energy.2016.11.089

[36] Thess, André. "Thermodynamic efficiency of pumped heat electricity storage." *Physical review letters* 111.11 (2013): 110602. https://doi.org/10.1103/PhysRevLett.111.110602

[37] White, A., Parks, G., & Markides, C. N. (2013). Thermodynamic analysis of pumped thermal electricity storage. *Applied Thermal Engineering*, *53*(2), 291-298.

[38] Schniewindt. Flow Heaters, https://www.schniewindt.de/en/csn-flow-heaters/; 2021 [accessed 05 Januar 2023]

[39] Ohmex. Electrical Process Flow Heaters datasheet, https://www.ohmex.de/en/wp-content/uploads/sites/3/2020/03/electric-process-heater_STR_2020-03.pdf; 2021 [accessed 05 Januar 2023]

[40] Belik, S.; Khater, O.; Zunft, S. Induction Heating of a Fluidized Pebble Bed: Numerical and Experimental Analysis. Appl. Sci. 2023, 13, 2311. https://doi.org/10.3390/app13042311

[41] Dreissigacker, V. Heat Mass Transfer (2017) 54: 955. https://doi.org/10.1007/s00231-017-2197-y

[42] T.E.W. Schumann, Heat transfer: a liquid flowing through a porous prism. J. Franklin Inst. 208 (1929) 405-416.

[43] McTigue JD, White AJ, Markides CN. Parametric studies and optimisation of pumped thermal electricity storage. Appl Energy 2015;137:800–11.

[44] Peters, Max S., Klaus D. Timmerhaus, and Ronald E. West. "Equipment costs-Plant design and economics for chemical engineers." (2002).

[45] Lucía O,Maussion P,Dede EJ,BurdíoJM(2014) Induction heating technology and its applications: past developments, current technology, and future challenges. IEEE Trans Ind Electron 61(5):2509– 2520

[46] Ergun S. Fluid flow through packed columns. Chem Eng Prog 1952;48:89–94.